

ZENN: A Thermodynamics-Inspired Computational Framework for Heterogeneous Data-Driven Modeling

Shun Wang^a, Shun-Li Shang^b, Zi-Kui Liu^{b,2}, and Wenrui Hao^{a,1}

This manuscript was compiled on May 14, 2025

Traditional entropy-based methods — such as cross-entropy loss in classification problems — have long been essential tools for quantifying uncertainty and disorder in data and developing artificial intelligence algorithms. However, the rapid growth of data across various domains has introduced new challenges, particularly the integration of heterogeneous datasets with intrinsic disparities. In this paper, we extend zentropy theory into the data science domain by introducing intrinsic entropy, enabling more effective learning from heterogeneous data sources. We propose a zentropy-enhanced neural network (ZENN) that simultaneously learns both energy and intrinsic entropy components, capturing the underlying structure of multi-source data. To support this, we redesign the neural network architecture to better reflect the intrinsic properties and variability inherent in diverse datasets. We demonstrate the effectiveness of ZENN on classification tasks and energy landscape reconstructions, showing its superior generalization capabilities and robustness—particularly in predicting high-order derivatives. As a practical application, we employ ZENN to reconstruct the Helmholtz energy landscape of Fe₃Pt using data generated from DFT and capture key material behaviors, including negative thermal expansion and the critical point in the temperature-pressure space. Overall, our study introduces a novel approach for data-driven machine learning grounded in zentropy theory, highlighting ZENN as a versatile and robust deep learning framework for scientific problems involving complex, heterogeneous datasets.

Zentropy-Enhanced Neural Network | Classification | Optimization | Data-driven modeling | Negative Thermal Expansion | Critical Temperature

The rise of complex, heterogeneous datasets is revolutionizing data science, unlocking new capabilities across fields such as biomedical modeling, materials discovery, climate prediction, and the development of digital twins. These digital replicas of physical systems rely on the seamless integration of real-time and historical data from multiple sources, including sensors, machines, experiments, and simulations (1–3). As a powerful paradigm for empirical discovery, data-driven modeling has been widely applied to solve inverse problems in physics (4), uncover biological mechanisms (5–7), and enable precision diagnostics for complex diseases (8, 9). A key tool in this modeling approach is entropy, a fundamental quantity in thermodynamics and information theory. Entropy provides a framework for modeling uncertainty, disorder, and irreversibility across a wide range of systems, from black holes (10, 11) and ecosystems (12) to digital infrastructures and quantum materials (13–15).

According to the second law of thermodynamics, internal processes in closed systems are irreversible, leading to positive entropy production (12, 16). However, traditional entropy-based methods tend to provide only macroscopic or microscopic approximations, often failing to account for internal disparities that arise when fusing multi-source data. These limitations are especially evident when integrating real-world datasets, which vary widely in scale, resolution, measurement conditions, and statistical properties. Such variability poses significant challenges for conventional machine learning techniques, which typically assume data homogeneity and stationarity (17). To overcome these challenges, zentropy theory introduces a robust thermodynamic framework that incorporates intrinsic entropy, capturing the variability across datasets due to environmental, experimental, or contextual differences (18, 19). This framework ensures thermodynamic consistency when integrating heterogeneous, real-time data in dynamic systems such as digital twins. Originally developed in 2008 to predict the magnetic phase diagrams of fcc-Ce (20) and L1₂-Fe₃Pt (21), zentropy theory has since been extended to a wide range of materials, including those with strong correlation effects (22–24), liquid and melting phases (25), plasticity (26), and superconductivity

Significance Statement

The increasing availability of complex, heterogeneous datasets poses significant challenges for traditional data-driven methods, which often assume data homogeneity and fail to account for internal disparities. Quantifying entropy and its evolution in such settings remains a fundamental problem in digital twins and data science. While traditional entropy-based approaches provide useful approximations, they are limited in handling multi-source, dynamically evolving systems. To address this, we introduce a zentropy-enhanced neural network (ZENN)—a novel framework that extends zentropy theory from quantum mechanics to data science by assigning intrinsic entropy to each dataset. ZENN is capable of learning both Helmholtz energy and intrinsic entropy, enabling robust generalization, accurate high-order derivative prediction, and adaptability to real-world data.

Author affiliations: ^aDepartment of Mathematics, Penn State University, University Park, Pennsylvania, United States of America; ^bDepartment of Materials Science and Engineering, Penn State University, University Park, Pennsylvania, United States of America

Author Contributions: Wenrui Hao and Zi-Kui Liu designed research; Shun Wang and Wenrui Hao contributed development of methodology; Shun Wang and Shun-Li Shang performed research; Shun Wang, Shun-Li Shang, Zi-Kui Liu and Wenrui Hao wrote the paper.

The authors have declared that no competing interests exist.

¹To whom correspondence should be addressed. E-mail: wxh64@psu.edu.

²To whom correspondence should be addressed. E-mail: zxl15@psu.edu.

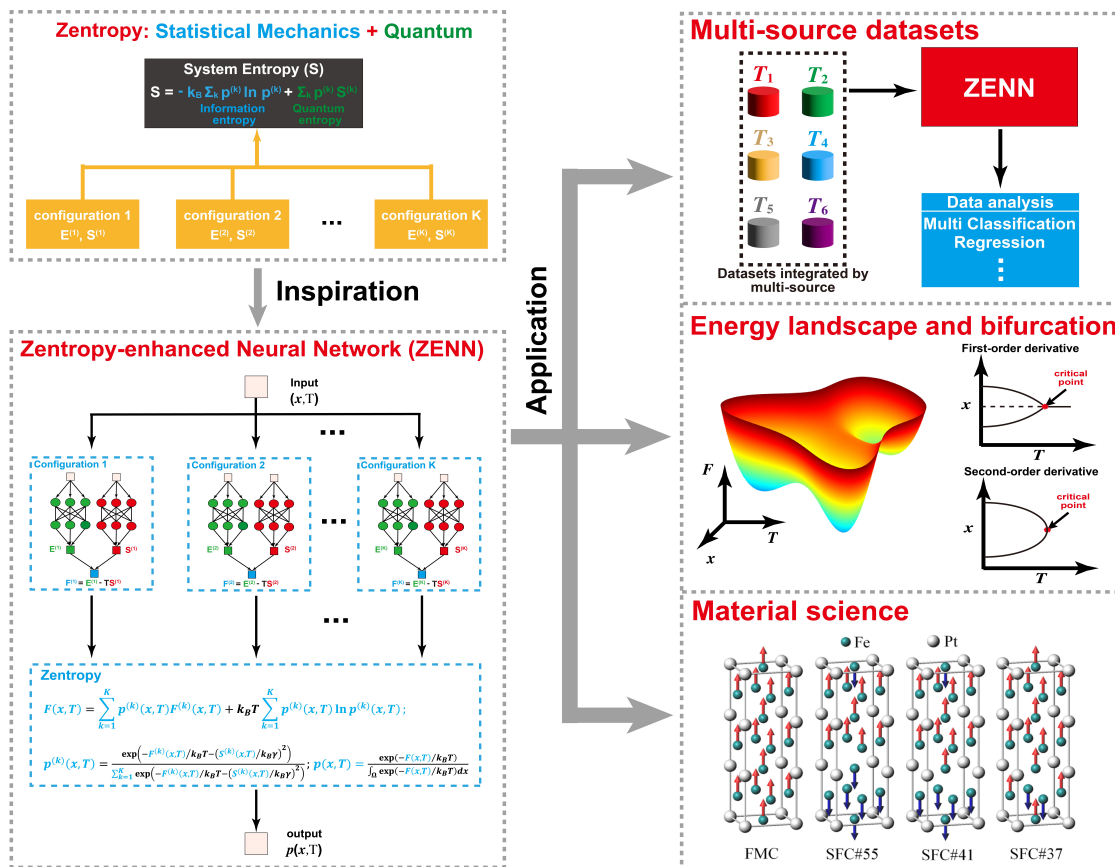


Fig. 1. Schematic of ZENN and its applications in different areas. Zentropy theory integrates statistical mechanics and quantum mechanics by assigning intrinsic entropy to each configuration in the system, thereby capturing internal disparities. By embedding zentropy theory into deep learning as a data-driven modeling framework, ZENN replaces the internal energy $E^{(k)}$ and entropy $S^{(k)}$ of each configuration with simple neural networks, and integrates information across all configurations through the total Helmholtz energy F . In this paper, ZENN has been applied to three representative tasks—multi-source data integration, energy landscape reconstruction, and inference of Fe_3Pt properties—demonstrating its potential as a powerful framework that effectively bridges statistical mechanics and machine learning.

(27). Despite its success in physics, zentropy’s reliance on density functional theory (DFT) for computing configuration-level entropy has limited its broader application to data-driven domains. However, as a foundational framework for integrating heterogeneous data, zentropy remains crucial for ensuring thermodynamic consistency and enabling more accurate, comprehensive models.

Unlike Shannon entropy, zentropy’s thermodynamic basis introduces domain-specific complexity. Meanwhile, the integration of thermodynamic concepts—such as entropy and energy—into deep learning has gained momentum across disciplines. For example, neural networks have been developed to construct DFT-based potential energy surfaces capable of capturing diverse bonding types (28). Noé et al. introduced Boltzmann Generators, embedding Boltzmann entropy into deep learning to predict protein structures (29). Thermodynamic principles have also enhanced interpretability in artificial intelligence (AI); for instance, the “Thermodynamics-Inspired Explainable Representations” framework uses interpretive entropy to produce model-agnostic, human-interpretable insights (30). Entropy production rate (EPR) has been incorporated into EPR-Net to model high-dimensional, non-equilibrium steady states (31), while Stochastic OnsagerNet learns macroscopic dynamics of dissipative systems from microscopic trajectories (32). Building on these innovations, we embed zentropy theory into deep learning as a backward modeling framework—extending its applicability beyond quantum and statistical mechanics and enabling entropy-aware learning from complex, heterogeneous data.

While zentropy has been widely used in forward modeling, where it plays a critical role in predicting system behavior, its integration into data-driven approaches for inverse problems remains unexplored. This paper addresses this gap by embedding zentropy theory into data science, advancing the application of entropy-based modeling within the context of data-driven techniques. More specifically, to broaden the applicability of zentropy theory beyond its traditional domain, we developed the Zentropy-Enhanced Neural Network (ZENN)—a framework designed to integrate multi-source data, reconstruct energy landscapes, and infer material properties. We benchmarked ZENN against conventional deep neural networks (DNNs) using illustrative models for three-class classification and energy landscape reconstruction. In both cases, ZENN consistently outperformed DNNs in terms of accuracy and stability. To further validate its capabilities, ZENN was applied to the Fe_3Pt compound, successfully capturing its negative thermal expansion (NTE) behavior and accurately predicting its critical point in the temperature-pressure space. These results demonstrate ZENN’s strong generalization ability and its enhanced performance in estimating high-order derivatives—an essential feature for modeling complex thermodynamic systems.

Results

Overview of ZENN and Its Applications. Zentropy theory states that the total entropy of a system comprises both the entropy of individual configurations and the statistical entropy across configurations. In forward problems, the Helmholtz free energy F of the system can be calculated if the

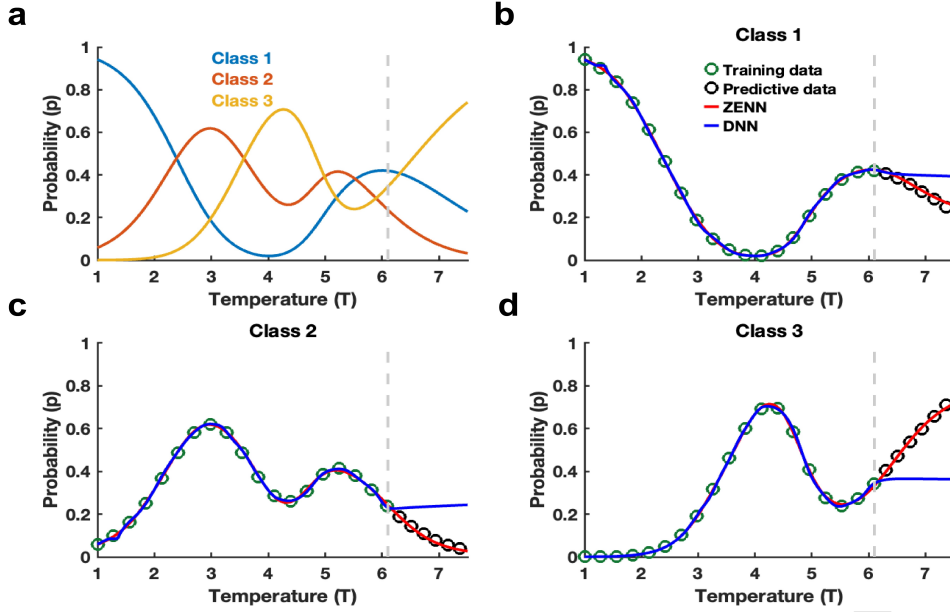


Fig. 2. Comparison of Predictive Performance Between ZENN and DNN in Classification. (a) Benchmark model for three-class classification. (b) Predictive probability of the first class. (c) Predictive probability of the second class. (d) Predictive probability of the third class. The green and black circles represent the training and test data, respectively. The dashed grey line indicates the boundary temperature separating the training and test data.

internal energy $E^{(k)}$, entropy $S^{(k)}$ of each configuration, and the number of configurations K are known (for details, see *Materials and Methods*). For materials applications, $E^{(k)}$ and $S^{(k)}$ are typically computed using density functional theory (DFT), while K is determined by the supercell size, reflecting the system's internal degrees of freedom.

In this paper, we introduce an inverse problem by recovering $E^{(k)}$ and $S^{(k)}$ and representing them with shallow neural networks (one or two hidden layers) by fitting the data. The number of configurations, K —analogous to the depth of a neural network—is incrementally increased until the loss converges (Fig. 1). Once $E^{(k)}$ and $S^{(k)}$ are determined via this data-driven approach, we apply entropy theory to compute the probability $p^{(k)}$ of each configuration and its corresponding Helmholtz free energy $F^{(k)}$. This enables us to reconstruct the systematic probability density p and the energy landscape F using ZENN (Fig. 1). By leveraging ZENN, we analyze multi-source data, encompassing classification tasks, and reconstruct the underlying energy landscape (Fig. 1). Furthermore, we identify critical points by applying automatic differentiation to the ZENN-reconstructed energy landscape, allowing us to compute the critical temperature T^* via Eq. (12).

ZENN Outperforms DNN in Multi-class Classification. We constructed a benchmark model for three-class classification to compare the performance of ZENN and multilayer neural networks. First, we defined the following three-class benchmark classification model:

$$f_k(T) = \begin{cases} 2.0 e^{-(T-2)^2} + 1.5 e^{-(T-6.0)^2}, & k = 1 \\ 2.5 e^{-(T-3)^2} + 1.2 e^{-(T-5.5)^2}, & k = 2 \\ 2.2 e^{-(T-4)^2} + 1.4 e^{-(T-6.5)^2}, & k = 3, \end{cases}$$

where T represents the temperature. The probability of each class, $p_k(T)$, is computed as

$$p_k(T) = \frac{f_k(T)}{\sum_{k=1}^3 f_k(T)}$$

for $k = 1, 2, 3$. As shown in Fig. 2a, the maximum predictive probability for each class varies with temperature T . For instance, when $T = 2$, the input is classified as the first class; when $T = 3$, it is classified as the second class; and when $T = 4$, it is classified as the third class. The samples, represented as one-hot vectors for class probabilities, were generated using the Monte Carlo method for different temperatures, denoted as (T_j, \mathbf{y}_j) (see Supplementary Materials for details).

For the three-class classification task, the number of configurations in ZENN was set to three ($K = 3$). Both the internal energy $E^{(k)}(T)$ and entropy $S^{(k)}(T)$ of each configuration in ZENN are modeled using neural networks with one hidden layer, each consisting of eight neurons, with T as the input. The DNN baseline was set to six hidden layers, each with eight neurons, ensuring the total number of neurons matched that of ZENN. Both models are trained using the Cross-Zentropy loss function as shown in Eq. (9), with $\hat{S} = 0$ for the DNN. The predictive probabilities of ZENN are computed using Eq. (6), while the probabilities of DNN are computed by setting $S^{(k)} = 0$, which is equivalent to the well-known softmax function.

On the training data, ZENN performs comparably to the DNN in predicting class probabilities, demonstrating strong approximation capabilities (Figs. 2b–d). However, on the test data, ZENN consistently outperforms the DNN when $T \geq 6$; for example, the DNN fails to identify the correct classification at $T = 7$ (Figs. 2b–d). This highlights ZENN's superior generalization ability and potential for reliable classification. The performance gap arises because the cross-entropy loss used in standard DNNs focuses solely on classification labels without directly capturing the underlying probability distribution. While a pure data-driven DNN can closely fit training data, it struggles to generalize. In contrast, ZENN incorporates zentropy, which enforces consistent and accurate probability computation in the cross-zentropy loss, thereby achieving both strong training performance and improved generalization.

Additionally, ZENN and DNN exhibit distinct thermodynamic behaviors across temperatures (Supplementary

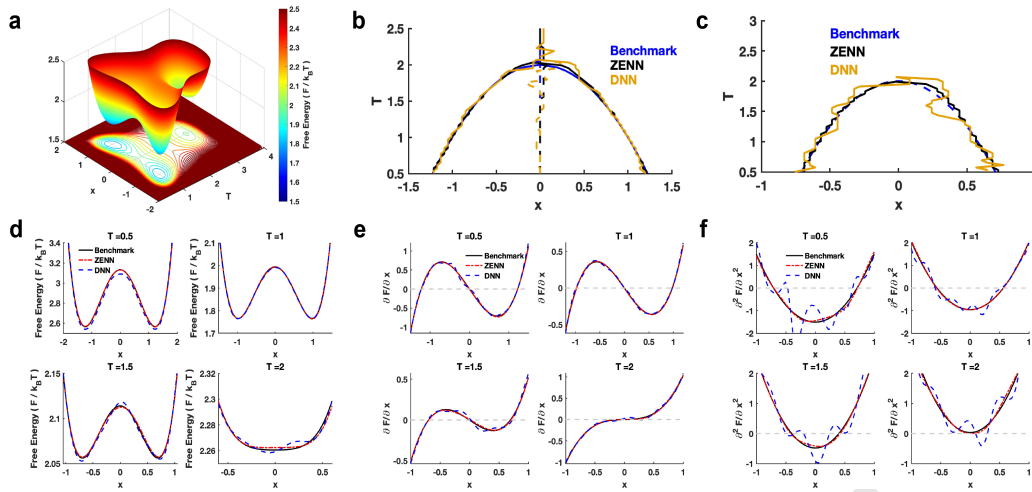


Fig. 3. Reconstruction of the Energy Landscape Using ZENN and DNN. (a) Energy landscape of the benchmark model. (b) Bifurcation diagram of x at different values of T . The dashed line represents the unstable state, while the solid line indicates the metastable state. (c) Zero-solution line of the second-order derivative $\frac{\partial^2 F}{\partial x^2} = 0$. The blue, black, and yellow lines represent the results from the benchmark model, ZENN, and DNN, respectively. (d) Helmholtz free energy $F/(k_B T)$ at four different values of T . Circles represent synthetic data generated from the Hill function. (e) First-order derivative $\frac{\partial F}{\partial x}$ at four different values of T . (f) Second-order derivative $\frac{\partial^2 F}{\partial x^2}$ at four different values of T . The black, blue, and red lines correspond to the benchmark model, ZENN, and DNN, respectively. The dashed grey line indicates the zero-solution line.

Fig. S6a). While both models predict stable internal energy at high temperatures, only ZENN integrates class-specific entropy to reconstruct the Helmholtz free energy for each class. This capability enables accurate class probability predictions in the high-temperature regime, highlighting ZENN's thermodynamic interpretability and predictive robustness (Supplementary Figs. S6d–e).

ZENN Reconstructs the Energy Landscape and Robustly Identifies Bifurcation Points. To further assess the applicability of ZENN, a benchmark model for the energy landscape was constructed. ZENN was then used to learn the configurations, reconstruct the energy landscape, and identify its bifurcation point, where the energy landscape changes. The benchmark model was defined as

$$F(x, T) = k_B T \left[\left(\frac{x^2}{2} + \frac{T-2}{2} \right)^2 + \frac{((T-2)^2 - 1)^2}{2} \right],$$

where k_B is the Boltzmann constant. As shown in Fig. 3a, when $T = 1$, the model has double wells. As T increases to 3, the double well degenerates into a single well. At $T = 2$, a saddle curve emerges, indicating that $T = 2$ is a bifurcation point for this benchmark model. This observation can be validated using both the first-order condition,

$$\left. \frac{\partial F}{\partial x} \right|_{T=2} = 0,$$

and the second-order condition,

$$\left. \frac{\partial^2 F}{\partial x^2} \right|_{T=2} = 0.$$

In ZENN, the internal energy $E^{(k)}(x, T)$ and entropy $S^{(k)}(x, T)$ for each configuration are modeled by neural networks with two hidden layers of eight neurons each, taking (x, T) as input. The number of configurations in ZENN was set to six ($K = 6$). The DNN was configured with four hidden layers, each containing 48 neurons, ensuring the total number

of neurons matched that of ZENN. Parameters for both ZENN and DNN were estimated using the Jensen–Shannon divergence (Eq. (10)). First- and second-order derivatives were computed via automatic differentiation in both ZENN and DNN (Figs. 3b–c).

The result of the Helmholtz energy $F/(k_B T)$ at $T = 2$ shows a significant difference between ZENN and DNN (Fig. 3d). The bifurcation diagram of x at different values of T , reconstructed by ZENN and DNN (Fig. 3b), shows that the first-order derivative from ZENN aligns more closely with the benchmark model than that from DNN. At all four different values of T , the first-order derivative of DNN exhibits fluctuations, though these have minimal impact on the bifurcation diagram (Fig. 3e). However, these fluctuations lead to inaccurate predictions of the second-order derivative. The zero-contour line of the second-order derivative (Fig. 3c) demonstrates that ZENN provides more robust high-order derivative predictions than DNN. At all four different values of T , the second-order derivative predicted by ZENN aligns well with the benchmark model, whereas DNN fails to predict both the second-order derivative and the correct number of zero crossings (Fig. 3f). These results underscore ZENN's robustness in high-order derivative estimation and its potential for identifying critical points where the energy landscape changes. While DNNs with L2 fitting are well-known to perform poorly in approximating derivatives, Sobolev training has been proposed to address this challenge by leveraging derivative information from the data (33). However, ZENN can effectively approximate derivatives using only the L2 fitting setup, demonstrating its superior ability to capture high-order derivatives without the need for additional derivative data.

Additionally, we evaluated the approximation capacity of ZENN on a more complex energy landscape to further demonstrate its robustness. Specifically, we constructed a two-dimensional energy landscape featuring three wells and illustrated ZENN's effectiveness in accurately capturing this landscape in Supplementary Fig. S4.

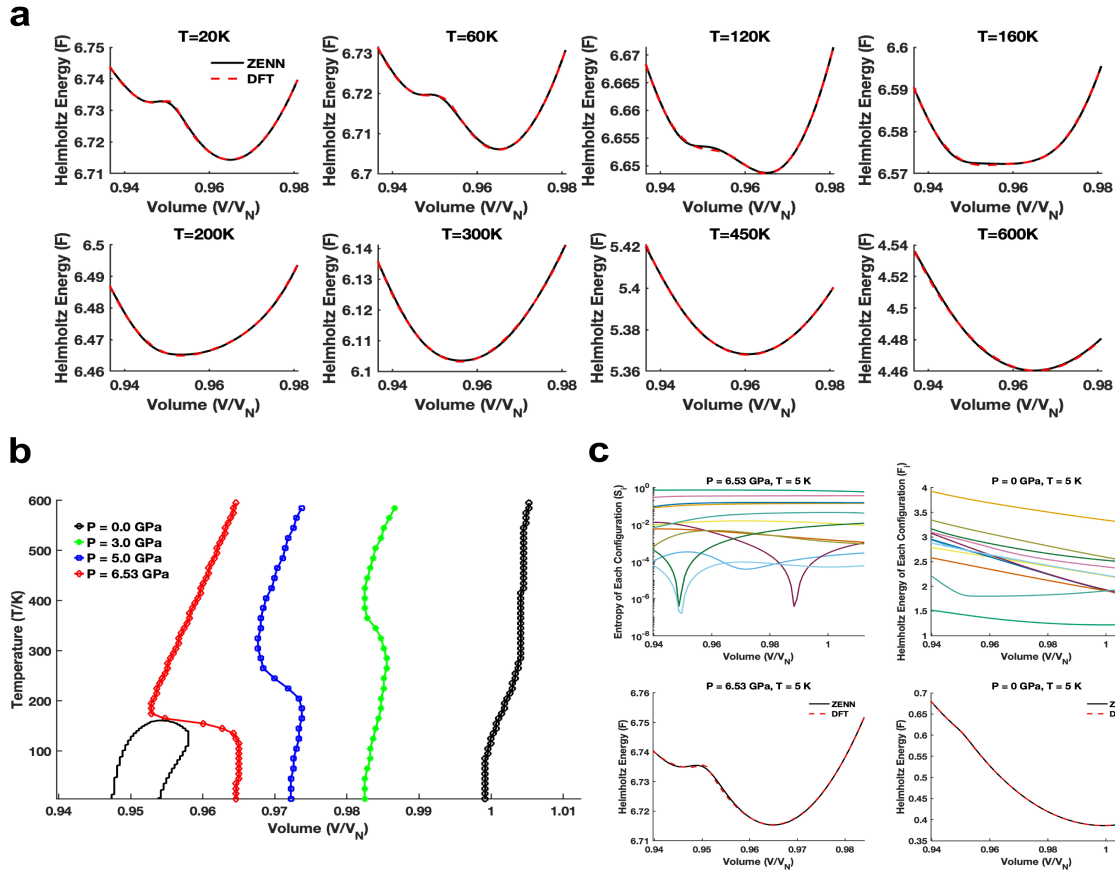


Fig. 4. ZENN-Based Identification of NTE and the Critical Temperature of Fe₃Pt. (a) Helmholtz energy of Fe₃Pt as a function of volume V at different temperatures T , under a pressure of 6.53 GPa. (b) Predicted T - V phase diagram of Fe₃Pt, showing isobaric volume curves, where the volume V is normalized to V_N at 298 K and 1 atm. (c) Entropy and Helmholtz energy of each configuration at $T = 5$ K. Colored lines represent the twelve configurations. Solid and dashed lines indicate the Helmholtz energy of Fe₃Pt predicted by ZENN and DFT, respectively.

ZENN Accurately Captures Negative Thermal Expansion and the Critical Point of Fe₃Pt.

We further applied ZENN to the Helmholtz energy data of Fe₃Pt generated by density functional theory (DFT) to assess its ability to predict material properties. A 12-atom $1 \times 1 \times 3$ supercell was employed, where nine Fe atoms possess spin-up and/or spin-down orientations, leading to $2^9 = 512$ total configurations, of which 37 are symmetry-independent. The DFT-based quasi-harmonic approximation (QHA), implemented in the VASP code (34), was used to compute the independent $F^{(k)}$ values, with full details provided in previous work (35). From these $F^{(k)}$ values, the total Helmholtz energy F of Fe₃Pt was calculated (Figs. 4a and S1 in Supplementary Materials; see Supplementary Materials for details).

In ZENN, both the internal energy $E^{(k)}(x, T)$ and entropy $S^{(k)}(x, T)$ of each configuration were modeled using neural networks with two hidden layers, each containing eight neurons. The number of configurations in ZENN was set to twelve ($K = 12$). By incorporating a convexity constraint into the Jensen–Shannon divergence loss function (Eq. (13)), ZENN’s predicted Helmholtz energy shows remarkable agreement with the DFT data across all temperatures (Fig. 4a and Supplementary Fig. S1).

Using ZENN, we computed the isobaric volume curves $\frac{\partial F}{\partial V} = -p$, the zero-solution line of the second-order derivative $\frac{\partial^2 F}{\partial V^2} = 0$, and the critical temperature T^* via Eq. (12). Under atmospheric pressure, ZENN accurately captures the negative thermal expansion (NTE), which becomes more pronounced with increasing pressure (Fig. 4b). At

6.53 GPa, ZENN predicts a critical temperature of 161 K (Fig. 4b), which aligns closely with the DFT-computed range of 160–165 K (Supplementary Fig. S2). These results are consistent with previous experimental and DFT-based studies (21, 36), demonstrating ZENN’s strong potential for predicting material properties.

It is important to note that some $S^{(k)}$ curves at 5 K and 6.53 GPa from ZENN (Fig. 4c) decrease with increasing volume and even exhibit sharp drops. These irregularities, when compared with DFT-based results, arise from certain combined configurations employed in ZENN. The intersection of Helmholtz energies for these combined configurations at specific volumes results in sharp fluctuations of $p^{(k)}$ values as well as sharp drops of $S^{(k)}$ values, as observed by ZENN at low temperatures (e.g., below 100 K, see Supplementary Fig. S7). For example, the sudden drop of $S^{(k)}$ around the normalized volume of 0.99 is primarily due to the abrupt predominance of ferromagnetic configuration (having the lowest entropy) in the combined configuration in ZENN. However, the total entropy from both ZENN and DFT shows similar trends as a function of volume, exhibiting a maximum point corresponding to NTE in Fe₃Pt (37). Additionally, one of the individual $S^{(k)}$ curves shows a large slope change with respect to volume (near 2 eV/atom in Fig. 4c) also due to the combination of different configurations utilized in ZENN. The Helmholtz energy of all configurations remains convex (Fig. 4c) at 5 K and 0 GPa. At both 0 GPa and 6.53 GPa, the total Helmholtz energy at 5 K predicted by ZENN shows excellent agreement with DFT results (Fig. 4c), further reinforcing ZENN’s applicability in materials science.

Discussions

In this study, we introduce and demonstrate ZENN, a data-driven framework grounded in zentropy theory that integrates neural networks with statistical mechanics to approximate energy landscapes, predict class probabilities, and identify critical transitions in material systems. By parameterizing the energy and entropy of individual configurations through compact neural networks, ZENN provides a systematic and interpretable approach for reconstructing Helmholtz free energy landscapes and capturing the complex thermodynamic behaviors of systems with multiple configurations. In contrast to conventional DNNs, where each layer is fully connected, ZENN models each configuration with a small, independent neural network, with the number of configurations roughly corresponding to the number of DNN layers. This design replaces strong nonlinearity across layers with physically grounded connections via thermodynamic principles, enhancing both robustness and derivative accuracy.

Our results across three applications—classification, energy landscape reconstruction, and property prediction for Fe₃Pt — demonstrate that ZENN consistently outperforms traditional DNNs. In classification tasks, ZENN achieves superior generalization by integrating intrinsic entropy contributions, a feature absent in conventional cross-entropy-based DNNs (Fig. 2). The cross-zentropy loss employed by ZENN simultaneously accounts for both energy and entropy, reducing overfitting and improving prediction reliability, particularly in heterogeneous or imbalanced datasets. This aligns with recent efforts in physics-informed machine learning, such as Sobolev training for derivative estimation (33) and Boltzmann generators for energy-based sampling, yet ZENN uniquely bridges these advances by explicitly modeling entropy fluctuations, enabling robust multi-source data integration.

In reconstructing energy landscapes, ZENN robustly predicts high-order derivatives and identifies bifurcation points that are typically inaccessible to conventional DNNs (Figs. 3c, f). While DNNs often require explicit derivative supervision to capture such behaviors, ZENN’s thermodynamic foundation ensures stable and physically consistent predictions of quantities like $\frac{\partial^2 F}{\partial x^2}$. This capability is particularly valuable in materials science, where subtle curvature changes in free energy landscapes govern phase transitions, such as magnetic ordering or negative thermal expansion. Notably, ZENN accurately predicted the critical temperature for Fe₃Pt, closely matching DFT and experimental results (Fig. 4b).

Beyond materials modeling, the ZENN framework is broadly applicable to other fields where energy landscapes or heterogeneous data distributions are central. Potential applications include protein folding in biophysics, climate data integration from satellite and ground measurements, and digital twins that fuse multi-resolution, real-time sensor data. ZENN’s ability to quantify and leverage intrinsic entropy differences offers a unique advantage in these contexts, ensuring consistent predictions across disparate datasets.

A key distinction between zentropy theory and classical Gibbs entropy lies in their treatment of configurational entropy. While Gibbs entropy adopts a top-down perspective based on probability distributions, zentropy theory integrates quantum and statistical mechanics to compute the total entropy from configuration-specific contributions, thereby im-

proving the accuracy of phase-transition predictions (18, 19). In forward modeling, zentropy theory requires evaluating all configurations—for example, 512 in Fe₃Pt—to capture behaviors like negative thermal expansion. In contrast, ZENN, as an inverse modeling framework, reconstructs the same energy landscape and predictive fidelity using as few as 12 configurations, demonstrating remarkable data efficiency.

Despite its advantages, ZENN’s current implementation requires predefining the number of configurations K , potentially limiting scalability for ultra-high-dimensional systems. Future extensions could explore adaptive or hierarchical configuration structures, or coupling ZENN with generative models and active learning frameworks to efficiently explore large configuration spaces. Additionally, while a convexity constraint was employed here for physical consistency in Fe₃Pt, other systems (e.g., glasses or non-equilibrium materials) may require alternative regularization schemes. Extending ZENN to dynamic systems with time-dependent entropy production would also unlock new applications in non-equilibrium thermodynamics and real-time monitoring.

In summary, ZENN represents a significant advancement in data-driven modeling by embedding thermodynamic laws directly into deep learning architectures. Its demonstrated success in classification, energy landscape reconstruction, and materials property prediction highlights the transformative potential of integrating domain-specific physics with modern machine learning. As complex, heterogeneous datasets become increasingly ubiquitous, ZENN’s interpretability, data efficiency, and robust handling of high-order derivatives position it as a powerful tool for accelerating discovery and design in materials science and beyond.

Materials and Methods

Zentropy through integration of Statistical and Quantum Mechanics. *Zentropy theory* (37) is fundamentally a multiscale entropy framework (19, 37, 38), where the “z” denotes the partition function, derived from the German word *zustandssumme*, meaning “sum over states.” This highlights that zentropy theory involves summing the entropies across multiple hierarchical levels. By integrating quantum mechanics and statistical mechanics (Fig. 1), zentropy theory (19) constructs a coarse-grained representation of entropy as follows:

$$S = \sum_{k=1}^K p^{(k)} S^{(k)} - k_B \sum_{k=1}^K p^{(k)} \ln p^{(k)} \quad [1]$$

where $S^{(k)}$ ($S^{(k)} \geq 0$) is the entropy of the k -th configuration. This is related to the degrees of freedom in vibrational frequencies of atoms in quantum mechanics (37). Here k_B is the Boltzmann constant and $p^{(k)}$ is the probability of the k -th configuration, which is inferred by the maximum entropy principle under the following three constraints:

$$\begin{cases} \sum_{k=1}^n p^{(k)} = 1 & \text{(Normalization)} \\ \sum_{k=1}^n p^{(k)} E^{(k)} = C_1 & \text{(Total internal energy constraint)} \\ \sum_{k=1}^n p^{(k)} (S^{(k)})^2 = C_2 & \text{(Entropy fluctuation constraint)} \end{cases}$$

where C_1 and C_2 are both constants. Whereas the first two constraints are standard in entropy-based modeling, we introduce the third constraint to quantify the fluctuation of

entropy across individual configurations, which effectively reflects the supercell size in DFT calculations. Thus, the optimization problem is summarized as:

$$\max_{p^{(k)}} S = \sum_{k=1}^K p^{(k)} S^{(k)} - k_B \sum_{k=1}^K p^{(k)} \ln p^{(k)} \quad [2]$$

s.t.

$$\sum_{k=1}^K p^{(k)} = 1, \quad \sum_{k=1}^K p^{(k)} E^{(k)} = C_1, \quad \sum_{k=1}^K p^{(k)} (S^{(k)})^2 = C_2$$

By introducing Lagrange multipliers λ_i ($i = 1, 2, 3$), the corresponding Lagrangian is given by:

$$\begin{aligned} \mathcal{L}(p^{(k)}) &= \sum_{k=1}^K p^{(k)} S^{(k)} - k_B \sum_{k=1}^K p^{(k)} \ln p^{(k)} \\ &- \lambda_1 \left(\sum_{k=1}^K p^{(k)} - 1 \right) - \lambda_2 \left(\sum_{k=1}^K p^{(k)} E^{(k)} - C_1 \right) \\ &- \lambda_3 \left(\sum_{k=1}^K p^{(k)} (S^{(k)})^2 - C_2 \right) \end{aligned} \quad [3]$$

Thus, the optimal solution satisfies:

$$\frac{\partial \mathcal{L}}{\partial p^{(k)}} = S^{(k)} - k_B (\ln p^{(k)} + 1) - \lambda_1 - \lambda_2 E^{(k)} - \lambda_3 (S^{(k)})^2 = 0 \quad [4]$$

which implies

$$p^{(k)} = \underbrace{\exp\left(-\frac{\lambda_1 + k_B}{k_B}\right)}_{\text{Normalization}} \underbrace{\exp\left(\frac{S^{(k)} - \lambda_2 E^{(k)}}{k_B}\right)}_{\text{Total internal energy}} \underbrace{\exp\left(-\frac{\lambda_3 (S^{(k)})^2}{k_B}\right)}_{\text{Fluctuation of intrinsic entropy}} \quad [5]$$

Due to the nondimensionalization of $p^{(k)}$, we set $\lambda_2 = \frac{1}{T}$ and $\lambda_3 = \frac{1}{\gamma^2 k_B}$, where γ is a tunable hyperparameter. Since the Helmholtz free energy of the k -th configuration is given by $F^{(k)} = E^{(k)} - TS^{(k)}$, the probability $p^{(k)}$ can be rewritten as:

$$\begin{aligned} p^{(k)} &= \frac{1}{Z} \exp\left(-\frac{F^{(k)}}{k_B T} - \left(\frac{S^{(k)}}{\gamma k_B}\right)^2\right), \\ Z &= \sum_{k=1}^K \exp\left(-\frac{F^{(k)}}{k_B T} - \left(\frac{S^{(k)}}{\gamma k_B}\right)^2\right). \end{aligned} \quad [6]$$

Thus, the total Helmholtz energy of system F is expressed as

$$\begin{aligned} F &= E - TS \\ &= \sum_{k=1}^K p^{(k)} E^{(k)} - T \left(\sum_{k=1}^K p^{(k)} S^{(k)} - k_B \sum_{k=1}^K p^{(k)} \ln p^{(k)} \right) \\ &= \sum_{k=1}^K p^{(k)} F^{(k)} + k_B T \sum_{k=1}^K p^{(k)} \ln p^{(k)} \end{aligned} \quad [7]$$

From Eq. (6), the partition function of the k -th configuration can be defined as $Z^{(k)} = \exp\left(-\frac{F^{(k)}}{k_B T} - \left(\frac{S^{(k)}}{\gamma k_B}\right)^2\right)$, which reduces to the standard definition in the forward-modeling of the zentropy theory when $\gamma k_B \gg S^{(k)}$, corresponding to relatively small fluctuations of the intrinsic entropy among configurations, as demonstrated for YNiO₃ (26). This formulation aligns with the classic principles of statistical mechanics developed by Gibbs, who considered systems as “of the same nature, but differing in the configurations and velocities which they have at a given instant” (39). In the present work for Fe₃Pt, a value $\gamma = 5$ was used.

Cross-zentropy Loss Function in Classification Tasks. The cross-entropy loss function is widely used in classification problems (40). We extend this framework to the zentropy setup and introduce the cross-zentropy loss function. Specifically, let $\mathbf{y}_i \in \mathbb{R}^K$ denote the true one-hot encoded label, $\mathbf{p}_i \in \mathbb{R}^K$ represent the predicted probability for class k , and K is the total number of classes. The loss function of cross-entropy, l_{CE} , is defined as:

$$l_{CE} = \frac{1}{M} \sum_{j=1}^M \langle \mathbf{y}_j, -\ln \mathbf{p}_j \rangle \quad [8]$$

where $\langle \cdot \rangle$ denotes the inner product, and M is the number of samples. This loss function quantifies the difference between the true labels and the predicted probabilities, penalizing incorrect classifications by increasing the loss value when the predicted probability diverges significantly from the true label.

To transition from cross-entropy to cross-zentropy loss, we introduce a modification to account for the intrinsic entropy approximation. Using Eq. (6), we modify the cross-entropy framework with zentropy theory, where the Helmholtz free energy of the i -th configuration is given by $F^{(k)} = E^{(k)} - TS^{(k)}$. Then the cross-zentropy loss function, l_{CZ} , is defined as:

$$l_{CZ}(\tilde{E}, \tilde{S}) = \frac{1}{M} \sum_{j=1}^M \left\langle \mathbf{y}_j, \frac{\tilde{E} - T_j \tilde{S}}{k_B T_j} + \left(\frac{\tilde{S}}{\gamma k_B}\right)^2 + \ln Z \right\rangle \quad [9]$$

$$Z = \sum_{k=1}^K \exp\left(-\frac{F^{(k)}}{k_B T_j} - \left(\frac{S^{(k)}}{\gamma k_B}\right)^2\right)$$

where $\tilde{E} = [E^{(1)}, E^{(2)}, \dots, E^{(K)}]$ denotes the internal energy of each class, $\tilde{S} = [S^{(1)}, S^{(2)}, \dots, S^{(K)}]$ denotes the entropy of each class, Z is chosen such that $\sum_{k=1}^K p^{(k)} = 1$, and K is the number of classes.

Jensen-Shannon divergence and Identification of critical point. When the data or distributions are continuous and defined over continuous variables, we employ Jensen-Shannon divergence in conjunction with ZENN to extend the framework. Specifically, the loss function is defined using the Jensen-Shannon divergence as follows:

$$\begin{aligned} &\min_{\{\theta_E^{(k)}, \theta_S^{(k)}\}_{k=1}^K} \mathcal{L}\left(\{\theta_E^{(k)}, \theta_S^{(k)}\}_{k=1}^K; x, T\right) \\ &= \frac{1}{2} \text{KL}(P||M) + \frac{1}{2} \text{KL}(Q||M), \quad \text{where } M = \frac{P+Q}{2} \end{aligned} \quad [10]$$

where P is the probability density of experimental data and Q is the probability density computed by the zentropy theory with $S^{(k)}(x, T)$ and $E^{(k)}(x, T)$. The parameters $\theta_S^{(k)}$ and $\theta_E^{(k)}$ are associated with the neural networks modeling $S^{(k)}(x, T)$ and $E^{(k)}(x, T)$, respectively. The Kullback–Leibler divergence (KL) is defined as follows:

$$\begin{aligned} \text{KL}(P\|M) &= \int_{\Omega} P(x, T) \ln P(x, T) dx \\ &\quad - \int_{\Omega} P(x, T) \ln M(x, T) dx, \\ \text{KL}(Q\|M) &= \int_{\Omega} Q(x, T) \ln Q(x, T) dx \\ &\quad - \int_{\Omega} Q(x, T) \ln M(x, T) dx. \end{aligned} \quad [11]$$

Identification of critical points. To identify the critical point of the energy landscape $F(x, T)$ using zentropy theory, we define the following zero-eigenvalue problem:

$$B(x^*, T^*, \xi) = \begin{cases} \nabla F(x^*, T^*) = 0, \\ \nabla^2 F(x^*, T^*) \xi = 0, \\ \|\xi\| = 1, \end{cases} \quad [12]$$

where ξ is the normalized eigenvector corresponding to the zero eigenvalue of the Hessian matrix $\nabla^2 F(x, T)$ of the energy landscape. This system allows us to identify the critical temperature T^* at which the energy landscape undergoes a stability change (41, 42).

Convexity constraint to Helmholtz energy of each configuration

Since each configuration of Fe₃Pt has a unique minimum on its Helmholtz energy (43), we introduce a convexity constraint on the Helmholtz energy for each configuration. This modification alters the loss function (Eq. (10)) as follows:

$$\begin{aligned} &\min_{\{\theta_E^{(k)}, \theta_S^{(k)}\}_{k=1}^K} \tilde{\mathcal{L}} \left(\{\theta_E^{(k)}, \theta_S^{(k)}\}_{k=1}^K; V, T \right) \\ &= \mathcal{L} \left(\{\theta_E^{(k)}, \theta_S^{(k)}\}_{k=1}^K; V, T \right) + \lambda \sum_{k=1}^K \int_{\Omega} \text{ReLU} \left(-\frac{\partial^2 F^{(k)}}{\partial V^2} \right) dV \end{aligned} \quad [13]$$

$$\text{ReLU}(x) = \begin{cases} x, & x \geq 0, \\ 0, & x < 0 \end{cases}$$

where λ is the regularization term and V denotes volume. With a fixed value of λ , we performed 30,000 epochs and minimized the loss. The optimal value of λ that minimizes the loss as much as possible was found to be 10^{-4} (44) (Supplementary Fig. S5).

Data and code availability. All relevant data are within the manuscript and its Supporting Information files. The public datasets are used in this study. Source codes and data have been deposited on the GitHub repository (<https://github.com/WilliamMoriarty/ZENN>).

Acknowledgments. This research supported by National Institute of General Medical Sciences through grant 1R35GM146894 (SW and WH), U.S. Department of Energy (DOE) through Grant No. DE-SC0023185, and the Endowed Dorothy Pate Enright Professorship at College of Earth and Mineral Science at the Pennsylvania State University (SLS and ZKL).

1. S Mihai, et al., Digital twins: A survey on enabling technologies, challenges, trends and future prospects. *IEEE Commun. Surv. & Tutorials* **24**, 2255–2291 (2022).
2. A Sharma, E Kosasih, J Zhang, A Brintrup, A Calinescu, Digital twins: State of the art theory and practice, challenges, and open research questions. *J. Ind. Inf. Integration* **30**, 100383 (2022).
3. EA Stahlberg, et al., Exploring approaches for predictive cancer patient digital twins: Opportunities for collaboration and innovation. *Front. Digit. Heal.* **4**, 1007784 (2022).
4. H Zheng, Y Huang, Z Huang, W Hao, G Lin, Homopins: Homotopy physics-informed neural networks for solving the inverse problems of nonlinear differential equations with multiple solutions. *J. Comput. Phys.* **500**, 112751 (2024).
5. NM Mirzaei, W Hao, L Shahriyari, Investigating the spatial interaction of immune cells in colon cancer. *Iscience* **26** (2023).
6. J Chen, H Huang, W Hao, J Xu, A machine learning method correlating pulse pressure wave data with pregnancy. *Int. journal for numerical methods biomedical engineering* **36**, e3272 (2020).
7. S Wang, W Hao, A systematic computational framework for practical identifiability analysis in mathematical models arising from biology. *arXiv preprint arXiv:2501.01283* (2025).
8. H Zheng, et al., Data-driven causal model discovery and personalized prediction in alzheimer's disease. *NPJ digital medicine* **5**, 137 (2022).
9. JR Petrella, et al., Personalized computational causal modeling of the alzheimer disease biomarker cascade. *The journal prevention Alzheimer's disease* **11**, 435–444 (2024).
10. SW Hawking, Black holes and thermodynamics. *Phys. Rev. D* **13**, 191 (1976).
11. SW Hawking, DN Page, Thermodynamics of black holes in anti-de sitter space. *Commun. Math. Phys.* **87**, 577–588 (1983).
12. U Seifert, From stochastic thermodynamics to thermodynamic inference. *Annu. Rev. Condens. Matter Phys.* **10**, 171–192 (2019).
13. J Quijano, H Lin, Entropy in the critical zone: a comprehensive review. *Entropy* **16**, 3482–3536 (2014).
14. P Tempesta, Beyond the shannon–khinchin formulation: The composability axiom and the universal-group entropy. *Annals Phys.* **365**, 180–197 (2016).
15. J Bhattacharya, M Nozaki, T Takayanagi, T Ugajin, Thermodynamical property of entanglement entropy for excited states. *Phys. review letters* **110**, 091602 (2013).
16. M Hillert, *Phase equilibria, phase diagrams and phase transformations: their thermodynamic basis.* (Cambridge university press), (2007).
17. Y Liu, et al., A digital twin-based assembly model for multi-source variation fusion on vision transformer. *J. Manuf. Syst.* **76**, 478–501 (2024).
18. ZK Liu, B Li, H Lin, Multiscale entropy and its implications to critical phenomena, emergent behaviors, and information. *J. Phase Equilibria Diffusion* **40**, 508–521 (2019).
19. ZK Liu, Thermodynamics and its prediction and calphad modeling: Review, state of the art, and perspectives. *Calphad* **82**, 102580 (2023).
20. Y Wang, et al., A thermodynamic framework for a system with itinerant-electron magnetism. *J. Physics: Condens. Matter* **21**, 326003 (2009).
21. Y Wang, S Shang, H Zhang, LQ Chen, ZK Liu, Thermodynamic fluctuations in magnetic states: Fe₃Pt as a prototype. *Philos. magazine letters* **90**, 851–859 (2010).
22. SL Shang, JE Saal, ZG Mei, Y Wang, ZK Liu, Magnetic thermodynamics of fcc ni from first-principles partition function approach. *J. applied physics* **108** (2010).
23. Y Wang, S Shang, X Hui, L Chen, Z Liu, Effects of spin structures on phonons in bafe₂as₂. *Appl. Phys. Lett.* **97** (2010).
24. JL Du, et al., Density functional thermodynamic description of spin, phonon and displacement degrees of freedom in antiferromagnetic-to-paramagnetic phase transition in ynio₃. *Mater. Today Phys.* **27**, 100805 (2022).
25. QJ Hong, ZK Liu, Generalized approach for rapid entropy calculation of liquids and solids. *Phys. Rev. Res.* **7**, L012030 (2025).
26. DL McDowell, ZK Liu, Hierarchical nonequilibrium thermodynamics of thermally activated dislocation plasticity of metals and alloys. *Int. J. Plast.* **188**, 104303 (2025).
27. ZK Liu, SL Shang, Revealing symmetry-broken superconducting configurations by density functional theory. *arXiv preprint arXiv:2404.00719* (2024).
28. J Behler, M Parrinello, Generalized neural-network representation of high-dimensional potential-energy surfaces. *Phys. review letters* **98**, 146401 (2007).
29. F Noé, S Olsson, J Köhler, H Wu, Boltzmann generators: Sampling equilibrium states of many-body systems with deep learning. *Science* **365**, eaaw1147 (2019).
30. S Mehdi, P Tiwary, Thermodynamics-inspired explanations of artificial intelligence. *Nat. Commun.* **15**, 7859 (2024).
31. Y Zhao, W Zhang, T Li, Epr-net: constructing a non-equilibrium potential landscape via a variational force projection formulation. *Nat. Sci. Rev.* **11**, nwa052 (2024).
32. X Chen, et al., Constructing custom thermodynamics using deep learning. *Nat. Comput. Sci.* **4**, 66–85 (2024).
33. WM Czarnecki, S Osindero, M Jaderberg, G Swirszcz, R Pascanu, Sobolev training for neural networks. *Adv. neural information processing systems* **30** (2017).
34. G Kresse, J Furthmüller, Efficient iterative schemes for ab initio total-energy calculations using a plane-wave basis set. *Phys. review B* **54**, 11169 (1996).
35. SL Shang, Y Wang, ZK Liu, Quantifying the degree of disorder and associated phenomena in materials through zentropy: Illustrated with invar fe₃pt. *Scripta Materialia* **225**, 115164 (2023).

36. ZK Liu, Y Wang, S Shang, Thermal expansion anomaly regulated by entropy. *Sci. reports* **4**, 7043 (2014).
37. ZK Liu, Y Wang, SL Shang, Zentropy theory for positive and negative thermal expansion. *J. Phase Equilibria Diffusion* **43**, 598–605 (2022).
38. ZK Liu, Quantitative predictive theories through integrating quantum, statistical, equilibrium, and nonequilibrium thermodynamics. *J. Physics: Condens. Matter* **36**, 343003 (2024).
39. JW Gibbs, *The Collected Works of J. Willard Gibbs: pt. 1. Elementary principles in statistical mechanics. pt. 2. Dynamics. Vector analysis and multiple algebra. Electromagnetic theory of light, etc.* (Longmans, Green) Vol. 2, (1902).
40. A Mao, M Mohri, Y Zhong, Cross-entropy loss functions: Theoretical analysis and applications in *International conference on Machine learning*. (PMLR), pp. 23803–23828 (2023).
41. W Hao, S Lee, YJ Lee, Companion-based multi-level finite element method for computing multiple solutions of nonlinear differential equations. *Comput. & Math. with Appl.* **168**, 162–173 (2024).
42. W Hao, C Xue, Spatial pattern formation in reaction–diffusion models: a computational approach. *J. mathematical biology* **80**, 521–543 (2020).
43. ZK Liu, Y Wang, *Computational thermodynamics of materials*. (Cambridge University Press), (2016).
44. CR Vogel, *Computational methods for inverse problems*. (SIAM), (2002).

DRAFT

ZENN: A Thermodynamics-Inspired Computational Framework for Heterogeneous Data-Driven Modeling

Shun Wang¹, Shun-Li Shang², Zi-Kui, Liu^{2,*} Wenrui Hao^{1,*}

Content

SECTION 1 DETAILS OF FIRST-PRINCIPLES CALCULATIONS AND FIRST-PRINCIPLES THERMODYNAMICS.....	1
SECTION 2 BENCHMARK MODEL OF TWO-DIMENSIONAL ENERGY LANDSCAPE	2
SECTION 3 NUMERICAL EXPERIMENTS	3
SECTION 4 SUPPLEMENTARY FIGURES.....	3
SECTION 5 SUPPLEMENTARY TABLES.....	6

Section 1 Details of first-principles calculations and first-principles thermodynamics

As detailed in (1), all DFT-based first-principles calculations of Fe₃Pt were performed by the Vienna *Ab initio* Simulation Package (VASP) (2). The ion-electron interaction was described by the projector augmented wave (PAW) method (3) and the exchange-correlation functional was described by the generalized gradient approximation (GGA) developed by Perdew, Burke, and Ernzerhof (PBE) (4). Regarding electron configurations, fourteen valence electrons (3p⁶3d⁷4s¹) were employed for Fe and ten (5d⁹6s¹) for Pt. During VASP calculations, a plane wave cutoff energy of 381 eV was used for structural relaxations by means of the Methfessel-Paxton method (5), and final calculations of total energy and electronic density of states were performed by the tetrahedron method with a Blöchl correction (6) using a plane wave cutoff energy of 520 eV. The employed *k*-point meshes for the 12-atom Fe₃Pt configurations were (14×14×4) and the self-consistency of total energy was converged to at least 10⁻⁵ eV/atom. Due to magnetic nature of Fe, all DFT-

based calculations were performed by the spin polarization calculations.

Helmholtz energy for configuration k , F^k , can be predicted by density functional theory (DFT) based quasiharmonic approach (QHA) with the contributions from vibrations $F_{vib}^k(V, T)$, thermal electrons $F_{el}^k(V, T)$, and the static total energy at 0 K, $E^k(V)$ (1, 7),

$$F^k(V, T) = E^k(V) + F_{vib}^k(V, T) + F_{el}^k(V, T) \quad (S1)$$

$E^k(V)$ of configuration k at 0 K can be determined by fitting the DFT calculated energy-volume (E - V) data points using a four-parameter Birch-Murnaghan equation of state (EOS) (7),

$$E^k(V) = a_1 + a_2 V^{-\frac{2}{3}} + a_3 V^{-\frac{4}{3}} + a_4 V^{-2} \quad (S2)$$

where a_1 , a_2 , a_3 , and a_4 are fitting parameters. Equilibrium properties from this EOS fitting include the equilibrium energy E_0 , volume V_0 , bulk modulus B_0 , and the pressure derivative of bulk modulus B' . Usually, eight reliable data points were employed for each EOS fitting in the present work, and the fitted equilibrium properties for these 37 independent configurations are shown in Table S1. To gain Helmholtz energy of each configuration k , we used the DFT-based QHA with vibrational contributions from the Debye model and thermal electron contributions from the Mermin statistics (7).

Section 2 Benchmark model of two-dimensional energy

landscape

We established the benchmark model of two-dimensional energy landscape $V(x_1, x_2)$ below:

$$V(x_1, x_2) = \sum_{i=1}^3 A_i \exp(-a_i(x_1 - x_{10i})^2 - b_i(x_2 - x_{20i})^2) \quad (S3)$$

Where the parameters are presented as:

$$A = [-3 \quad -3 \quad -3];$$

$$a = [3 \quad 3 \quad 3];$$

$$b = [3 \quad 3 \quad 3];$$

$$x_{10} = [-1 \quad 1 \quad 0];$$

$$x_{20} = [0 \quad 0 \quad 1.5].$$

Herein, both Boltzmann constant k_B and temperature T are set to 1.0.

Section 3 Numerical Experiments

For training, the activation function is $\text{Tanh}()$, and we use **Adam** as the optimizer with a learning rate 10^{-2} . Both DNNs and ZENN are trained for 20000 epochs in most of the examples, unless otherwise specified. Other parameters are shown in Table S2.

Section 4 Supplementary Figures

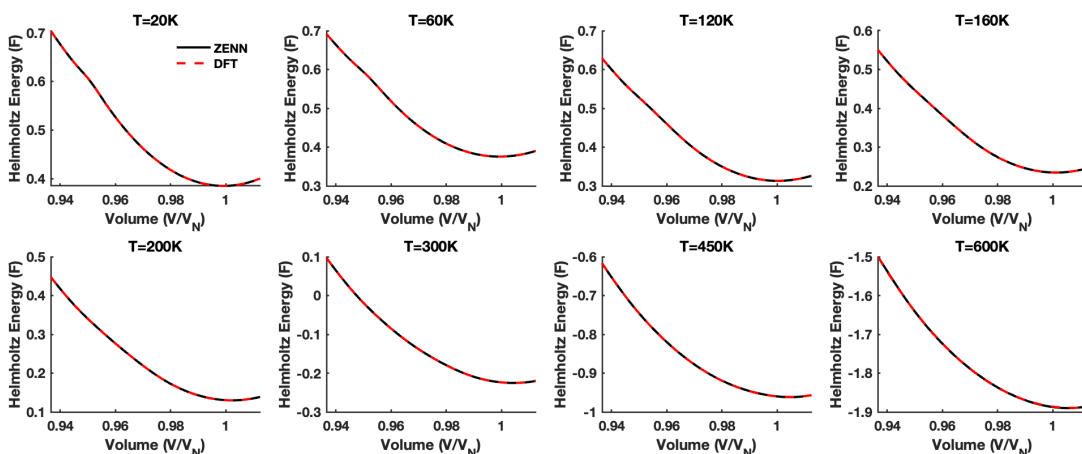


Fig. S1. Helmholtz energy of Fe_3Pt with the volume V at the different temperatures T , with atmospheric pressure.

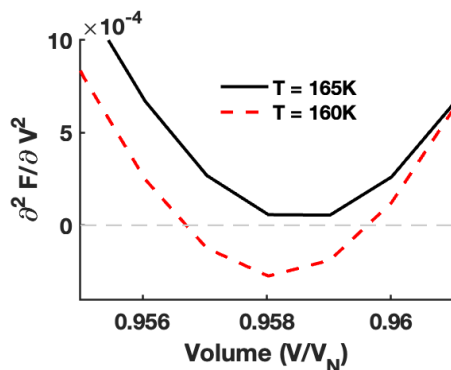


Fig. S2. Second-order derivative to Helmholtz energy of Fe_3Pt with the volume V at $T = 160\text{ K}$ and $T = 165\text{ K}$

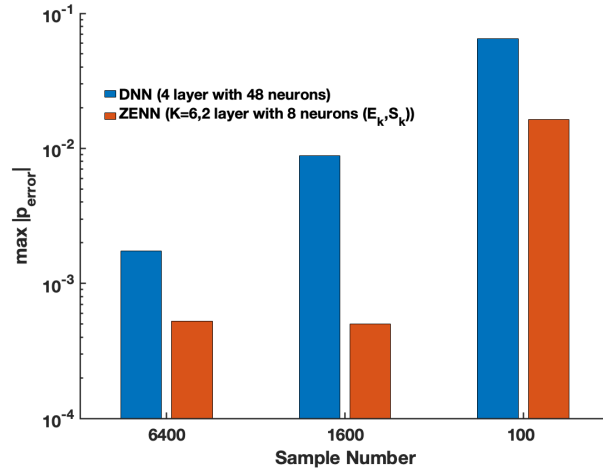


Fig. S3. Comparison of Generalization Between DNN and ZENN. $\max |p_{error}|$ denotes the maximum prediction error over the prediction set, which consists of 10,000 samples arranged in a 100×100 grid.

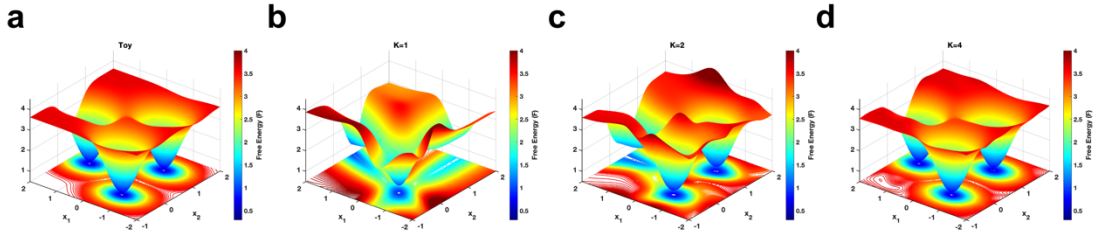


Fig. S4. Approximation capacity of ZENN with respect to the number of configurations. Benchmark model of two-dimensional energy landscape is presented in section 2.

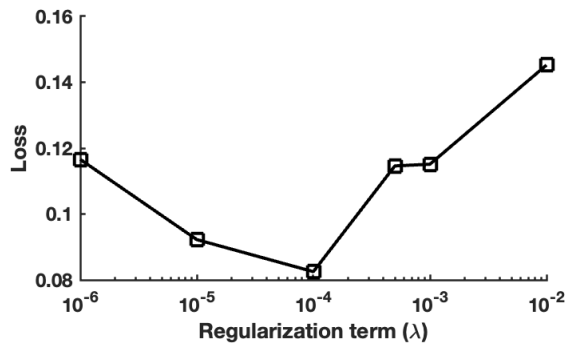


Fig. S5. Regularization term λ associated with the loss function Eq. (13).

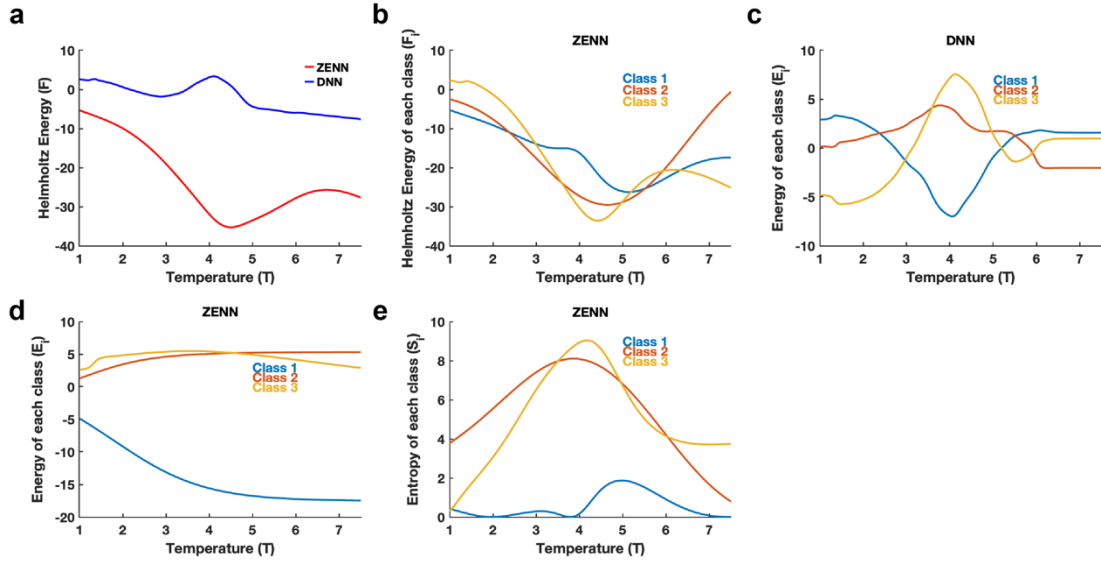


Fig. S6. Helmholtz Energy of ZENN and DNN in Multiclass Classification Task. a. Helmholtz energy of ZENN and DNN. b. Helmholtz energy of each class in ZENN. c. Energy of each class in DNN. d. Energy of each class in ZENN. e. Entropy of each class in ZENN.

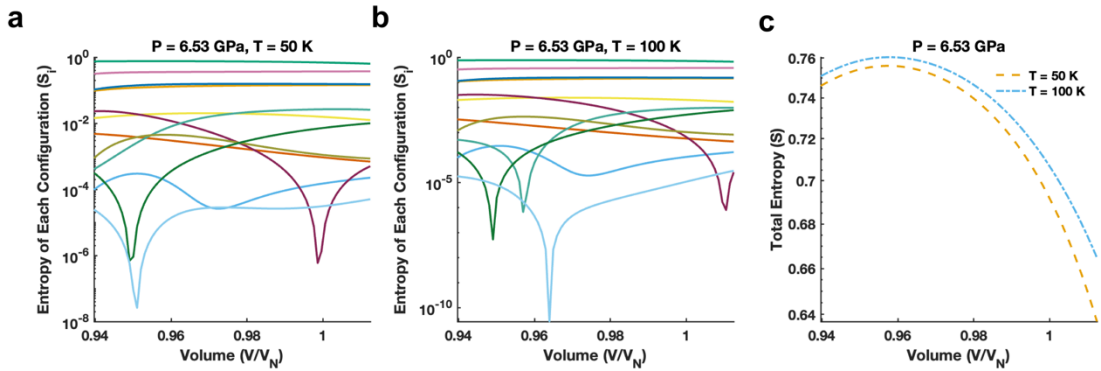


Fig. S7. Entropy of Fe₃Pt computed by ZENN. a. Entropy of each configuration at $P = 6.53$ GPa and $T = 50$ K. b. Entropy of each configuration at $P = 6.53$ GPa and $T = 100$ K. c. Total Entropy at $P = 6.53$ GPa. Blue dotted and orange dashed line represents $T = 100$ K and $T = 50$ K, respectively.

Section 5 Supplementary Tables

Table S1. Fitted equilibrium properties by Eq. (S2) for Fe₃Pt using the 12-atom supercell, including V_0 , E_0 , B_0 , and B' . Here, configuration #1 is the ferromagnetic configuration, “DF” indicates degeneracy factor for each configuration with the total degeneracy factors of 512 (2^9) due to 9 spin up and spin down Fe atoms. Note that these results are also reported in (1).

Configuration	DF	V_0 (Å ³ /atom)	E_0 (eV/atom)	B_0 (GPa)	B'
1	2	13.124	0.0000	177.01	3.447
2	6	12.901	0.0122	163.06	4.260
3	12	12.910	0.0160	162.96	4.440
4	12	13.002	0.0191	171.16	3.501
5	6	13.005	0.0202	171.75	3.271
6	6	12.929	0.0211	164.05	3.740
7	24	12.890	0.0281	162.43	3.923
8	24	12.947	0.0291	164.33	3.159
9	12	12.875	0.0372	164.70	4.059
10	12	12.868	0.0419	170.28	4.144
11	12	12.867	0.0422	171.76	3.721
12	24	12.840	0.0455	161.43	3.772
13	6	12.767	0.0457	161.03	4.388
14	12	12.859	0.0462	163.01	3.224
15	12	12.864	0.0467	168.31	4.357
16	24	12.801	0.0491	167.54	4.154
17	24	12.804	0.0493	165.12	4.649
18	12	12.765	0.0494	157.04	4.507
19	24	12.789	0.0505	169.38	4.816
20	12	12.833	0.0517	169.08	4.029
21	6	12.834	0.0521	164.59	3.891
22	6	12.747	0.0533	163.93	4.670
23	24	12.765	0.0551	159.41	4.137
24	12	12.724	0.0559	170.18	4.298
25	24	12.715	0.0586	172.04	4.622
26	24	12.779	0.0593	167.06	4.309
27	24	12.788	0.0596	170.54	4.187
28	12	12.727	0.0599	164.79	4.109
29	24	12.806	0.0623	169.21	4.052
30	12	12.703	0.0686	174.20	4.283
31	12	12.729	0.0712	169.24	4.215
32	12	12.740	0.0733	165.45	4.122
33	12	12.716	0.0877	163.09	3.917
34	12	12.754	0.0895	162.97	3.933
35	2	12.684	0.0899	167.31	4.483
36	4	12.681	0.0900	167.39	4.735

Table S2. Hyperparameters in ZENN.

	k_B	γ
Classification	1.0	5.0
Energy landscape	1.0	5.0
Fe ₃ Pt	0.1	5.0

Table S3. Pseudocode for Generating Data in a Three-Class Benchmark Model

Algorithm: Generating Data in a Three-Class Benchmark Model

1. Initialize parameters:
 - num_elements \leftarrow 3
 - T_values \leftarrow 100 values linearly spaced from 1 to 8
 - p_matrix \leftarrow zeros matrix of size (3 \times 100)
 2. Compute multi-modal probability functions for each T:
 - For each T in T_values:
 - f1(T) \leftarrow Gaussian peak at T=2 and T=6 (weighted sum)
 - f2(T) \leftarrow Gaussian peak at T=3 and T=5.5
 - f3(T) \leftarrow Gaussian peak at T=4 and T=6.5
 - Normalize:
 - Z(T) \leftarrow f1 + f2 + f3
 - P1(T) \leftarrow f1 / Z
 - P2(T) \leftarrow f2 / Z
 - P3(T) \leftarrow f3 / Z
 - Store [P1; P2; P3] in p_matrix
 3. Sample selected T indices:
 - t \leftarrow select every 4th index from 1 to 100
 - TT \leftarrow corresponding temperature values from T_values(t)
 4. Initialize data \leftarrow empty matrix
 5. For each selected T (indexed by t):
 - n \leftarrow 10,000
 - Generate n random class labels (1, 2, or 3) according to probabilities p_matrix(:, t(j))
 - For each label:
 - Convert to one-hot encoded vector (length = 3)
 - Append the corresponding T value (TT(j)) as an extra column
 - Stack the one-hot data with T into `data` matrix
 6. Final output:
 - data is an [n \times 4] \times num_T matrix with columns:
 - [one-hot class label (3 cols), T value (1 col)]
-

References

1. S.-L. Shang, Y. Wang, Z.-K. Liu, Quantifying the degree of disorder and associated phenomena in materials through zentropy: Illustrated with Invar Fe₃Pt. *Scripta Materialia* 225, 115164 (2023).
2. G. Kresse, J. Furthmüller, Efficient iterative schemes for *ab initio* total-energy calculations using a plane-wave basis set. *Physical Review B* 54, 11169–11186 (1996).
3. G. Kresse, D. Joubert, D. Kresse, G. Joubert, From ultrasoft pseudopotentials to the projector augmented-wave method. *Physical Review B* 59, 1758–1775 (1999).
4. J. P. Perdew, K. Burke, M. Ernzerhof, Generalized gradient approximation made simple. *Physical Review Letters* 77, 3865–3868 (1996).
5. M. Methfessel, A. T. Paxton, High-precision sampling for Brillouin-zone integration in metals. *Physical Review B* 40, 3616–3621 (1989).
6. P. E. Blöchl, O. Jepsen, O. K. Andersen, Improved tetrahedron method for Brillouin-zone integrations. *Physical Review B* 49, 16223–16233 (1994).
7. S.-L. Shang, Y. Wang, D. Kim, Z.-K. Liu, First-principles thermodynamics from phonon and Debye model: Application to Ni and Ni₃Al. *Computational Materials Science* 47, 1040–1048 (2010).